International Journal of
Molecular Sciences

MDPI

Article

Optical and Material Characteristics of MoS_2/Cu_2O Sensor for Detection of Lung Cancer Cell Types in Hydroplegia

Arvind Mukundan [1], Shih-Wei Feng [2], Yu-Hsin Weng [1], Yu-Ming Tsao [1], Sofya B. Artemkina [3,4], Vladimir E. Fedorov [3,4], Yen-Sheng Lin [5], Yu-Cheng Huang [6,*] and Hsiang-Chen Wang [1,*]

1 Department of Mechanical Engineering, Advanced Institute of Manufacturing with High Tech Innovations (AIM-HI), Center for Innovative Research on Aging Society (CIRAS), National Chung Cheng University, 168, University Rd., Min Hsiung, Chia Yi 62102, Taiwan; d09420003@ccu.edu.tw (A.M.); soul_loving0629@yahoo.com.tw (Y.-H.W.); d09420002@ccu.edu.tw (Y.-M.T.)
2 Department of Applied Physics, National University of Kaohsiung, 700 Kaohsiung University Rd., Nanzih District, Kaohsiung 81148, Taiwan; swfeng@nuk.edu.tw
3 Nikolaev Institute of Inorganic Chemistry, Siberian Branch of Russian Academy of Sciences, 630090 Novosibirsk, Russia; artem@niic.nsc.ru (S.B.A.); fed@niic.nsc.ru (V.E.F.)
4 Department of Natural Sciences, Novosibirsk State University, 1, Pirogova str., 630090 Novosibirsk, Russia
5 Department of Electronic Engineering, I-Shou University, No. 1, Sec. 1, Syuecheng Rd., Dashu District, Kaohsiung 84001, Taiwan; yslin@isu.edu.tw
6 Department of Dentistry, Kaohsiung Armed Forces General Hospital, 2, Zhongzheng 1st. Rd., Kaohsiung 80284, Taiwan
* Correspondence: tim1018@hotmail.com (Y.-C.H.); hcwang@ccu.edu.tw (H.-C.W.)

check for updates

Citation: Mukundan, A.; Feng, S.-W.; Weng, Y.-H.; Tsao, Y.-M.; Artemkina, S.B.; Fedorov, V.E.; Lin, Y.-S.; Huang, Y.-C.; Wang, H.-C. Optical and Material Characteristics of MoS_2/Cu_2O Sensor for Detection of Lung Cancer Cell Types in Hydroplegia. *Int. J. Mol. Sci.* **2022**, *23*, 4745. https://doi.org/10.3390/ijms23094745

Academic Editor: Raghvendra Singh Yadav

Received: 4 April 2022
Accepted: 22 April 2022
Published: 25 April 2022

Abstract: In this study, n-type MoS_2 monolayer flakes are grown through chemical vapor deposition (CVD), and a p-type Cu_2O thin film is grown via electrochemical deposition. The crystal structure of the grown MoS_2 flakes is analyzed through transmission electron microscopy. The monolayer structure of the MoS_2 flakes is verified with Raman spectroscopy, multiphoton excitation microscopy, atomic force microscopy, and photoluminescence (PL) measurements. After the preliminary processing of the grown MoS_2 flakes, the sample is then transferred onto a Cu_2O thin film to complete a p-n heterogeneous structure. Data are confirmed via scanning electron microscopy, SHG, and Raman mapping measurements. The luminous energy gap between the two materials is examined through PL measurements. Results reveal that the thickness of the single-layer MoS_2 film is 0.7 nm. PL mapping shows a micro signal generated at the 627 nm wavelength, which belongs to the B2 excitons of MoS_2 and tends to increase gradually when it approaches 670 nm. Finally, the biosensor is used to detect lung cancer cell types in hydroplegia significantly reducing the current busy procedures and longer waiting time for detection. The results suggest that the fabricated sensor is highly sensitive to the change in the photocurrent with the number of each cell, the linear regression of the three cell types is as high as 99%. By measuring the slope of the photocurrent, we can identify the type of cells and the number of cells.

Keywords: photoelectrochemical; chemical vapor deposition; molybdenum disulfide (MoS_2); cuprous oxide (Cu_2O); positive oxide trap state; DNA; biosensor

1. Introduction

Molybdenum disulfide (MoS_2) is one of the two-dimensional (2D) transition metal chalcogenides that have been studied recently [1–6]. Materials related to nanometer-scale electronic and optoelectronic components, such as field-effect transistors, prospective memory components, light-emitting diodes (LED), and sensors, have been manufactured because of the excellent spin-valley coupling and flexural and optoelectronic properties of MoS_2 [7–19]. However, MoS_2 is a layered structure, which has good lubricity, resistance to pressure, and wear resistance, and is mostly used as solid lubricant [20]. It is used in equipment operating under high-speed, heavy-load, high-temperature, and chemical

corrosive conditions. MoS_2 is a black hexagonal crystal structure with silver-gray luster, its Moiré mass is 160.07 g/mol, density is 5.06 g/cm^3, and melting point is 1185 °C. MoS_2 itself is insoluble in water, generally insoluble in other acids, alkalis, and organic solvents. However, at 400 °C, oxidation occurs slowly, and molybdenum trioxide (MoO_3) gradually forms. PN heterostructures have been widely used in the semiconductor industry; as a typical P-type semiconductor, Cu_2O is considered to be the most effective material [21]. With these characteristics, Cu_2O can be effectively used as an absorption layer in the visible wavelength range [22–25]. In a bulk MoS_2 semiconductor, an indirect energy gap of 1.2 eV between the G- and S-point conduction bands, and a single-layer MoS_2 semiconductor has a direct energy gap of 1.84 eV. Studies on light absorption, light reflection, and light excitation spectroscopy have evolved from bulk materials to single-layer TMDs [26]. In 2014, Yu-Fei Zhao et al. used a simple chemical synthesis method to cover MoS_2 successfully on p-Cu_2O semiconductors for high-efficiency solar hydrogen production [21]. In 2016, Xinne Zhao et al. assembled Cu_2O nanoparticles and MoS_2 nanosheets with a 2D planar structure into a 3D MoS_2/Cu_2O porous nanocomposite through hydrothermal synthesis [27,28]. In 2017, Linxia Fang et al. successfully decorated Cu_2O nanoparticles on flower-like MoS_2 and used them for non-enzymatic current detection in glucose. This structure has Cu_2O nanoparticles dispersed in MoS_2 [29]. Gang Li et al. reported the hydrothermal synthesis of MoS_2/Cu_2O nanocomposites with a tunable heterojunction to enhance the photochemical activity and stability of visible light [30]. The lack of energy gap of graphene in two-dimensional materials has shifted the focus on two-dimensional transition metal dichalcogenides (TMDs) with different energy gaps obtained by changing the number of layers. In the review of previous studies on MoS_2/Cu_2O, MoS_2/Cu_2O has high-performance photocatalysis, excellent electrocatalysis, strong stability, reproducibility, and high selectivity for non-MEI sensors. This structure can be used as a hydrogen oxide biosensor for environmental engineering applications, such as energy storage and water purification. It can also be used as a non-MEI current detection in glucose oxidation. It is better for the signal interference of uric acid, dopamine, and ascorbic acid. Apart from inorganic biosensors, organic materials are also getting attention in the last few years. Some biosensors using poly(methylene blue) (PMB), poly(alizarin yellow R), poly(azure A), poly(azure B), poly(azure C), poly(brilliant cresyl blue), and poly(thionine) has been widely studied and reported [31–37]. Even though these biosensors have good selectivity, their disadvantages include instability, cost, and a need for a mediator in some cases [38]. On the other hand, in recent years due to the excellent electrochemical properties of Cu_2O, much research has been conducted towards its application as a sensor [39–42]. MoS_2 which has a similar structure to graphene due to its conductivity and good electrical and chemical properties has been widely reported to be employed in numerous biosensors [43–45].

Hence, in this research, a new MoS_2/Cu_2O PN heterojunction structure, can reduce the predominant disadvantage of noise interference to the detection signal through different growth methods, material special characteristics, and the structure itself. This MoS_2/Cu_2O structure is applied to a sensor for cancer cells with different canceration levels. In this study, CVD is conducted for single-layer MoS_2 to obtain large-area and uniform MoS_2 films. Several measurement techniques, including Raman mapping, are used to check the number of layers. Atomic force microscopy (AFM) is employed for thickness analysis and scanning electron microscopy (SEM) is utilized to observe surface morphology. X-ray diffraction (XRD; Figure S1 for XRD) is conducted to measure whether a signal appears, and transmission electron microscopy (TM; Figure S4) is performed to determine the direction of the crystal lattice. However, studies on the synthesis of semiconductor materials and nanostructures have also been carried out. During the research, Cu_2O nanostructures have been successfully fabricated through electrochemical deposition. The major application of this heterostructure is to develop a low-cost and rapid way to detect lung cancer cell types in hydroplegia by fabricating a PEC biosensor that is highly sensitive to lung cancer cells significantly reducing the current busy procedures and longer waiting time for detection.

2. Materials and Methods

The glass substrate used in the experiment was indium tin oxide (ITO) for Cu_2O electroplating. The resistance of the ITO surface was 7 Ω, and the thickness of the coating was 200 nm. All the chemicals used were all American Chemical Society (ACS) and guaranteed reagent (GR) to avoid the failure of results because of insufficient purity or residual impurities in the grown crystals, especially low-chlorine Sigma-Aldrich (Burlington, MA, USA) 98+% for sodium hydroxide because the solution of Cu_2O deposition was susceptible to the influence of chloride ions to produce copper chloride precipitation.

2.1. Process and Steps of Electrochemical Cu_2O Growth

2.1.1. Substrate and Electrolysis Pretreatment

Cu_2O was prepared through electrochemical deposition, and the substrate used was a 2 cm × 2 cm transparent conductive film made of ITO for Cu_2O electroplating (Supplementary Section S1.1 for the Material characteristics of Cu_2O). P-type Cu_2O has a small energy gap of 2.0 eV, which was a suitable conduction band [46,47]. Acetone, methanol, isopropanol, and deionized water were used to reduce the impurities, such as dust, oil stains, or residues, on the electrode surface after ITO plating. The adhesion of impurity contamination also improved the stability of film growth to obtain a higher-quality Cu_2O film (Supplementary Section S3 for the List of substrates, organic solvents, gases, and chemicals used to grow Cu_2O and MoS_2). In the cleaning steps, the electrode surface was first cleaned with acetone in an ultrasonic oscillator for 10 min to dissolve and remove surface oil stains or other organic impurities. After the specimen was shaken and washed with acetone, it was rinsed with methanol in an ultrasonic oscillator for 10 min to dissolve and remove residual copper contamination on the surface. Isopropanol was used for cleaning in an ultrasonic oscillator for 10 min to dissolve and remove surface oil stains or other organic impurities. The glass substrate was soaked in deionized water with a resistivity of 18.2 M W·cm (25 °C), and an ultrasonic oscillator was used for 10 min to remove residual organic solvents. The sample was taken out, and a high-pressure nitrogen gun was used to remove the moisture on the surface of the ITO glass substrate. The ITO glass substrate was baked in an oven at 100 °C for 30 min to remove the residual moisture on the substrate and placed in a clean moisture-proof box for later use. The cut graphite rods with a diameter of 1 cm and a length of 18 cm were subjected to electrochemical Cu_2O deposition. The main purpose of cleaning the electrodes of the graphite rods was to reduce impurities, such as dust, oil stains, and residual powder, on the electrode surface during graphite rod production. External impurities contaminated Cu_2O electrolytic deposition and improved film growth stability. For cleaning, the graphite rod was soaked in 1 M sodium hydroxide solution and washed with ultrasonic vibration for 30 min to remove grease and organic pollutants adsorbed on the surface. The surface of the graphite rod was ground with sandpaper and rinsed with deionized water during grinding to remove the powder remaining in the graphite rod manufacturing. The graphite rod was soaked in deionized water and shaken for 30 min with ultrasonic cleaning to reduce the residual impurities on the surface. The graphite rod was baked in an oven at 100 °C for 30 min to remove the surface moisture and placed in a moisture-proof box to complete the pretreatment of the graphite electrode.

2.1.2. Preparation of Cu_2O Film

A Cu_2O thin film was prepared for electrochemical deposition to grow a highly uniform thin film on the ITO glass substrate (Supplementary Section S1.2 for Cu_2O Synthesis). The electrolyte was made of 0.4 M copper sulfate powder ($CuSO_4$), 85% lactic acid, and 5 M sodium hydroxide (NaOH) prepared into a 1000 c.c. aqueous solution. The pH could be adjusted to 10, 11, and 12 through the amount of sodium hydroxide, which was measured in real time by a portable Starter300 pH meter (ST300). A DC power supply (MOTECH LPS505N) was used to power the two-pole electrochemical deposition system equipment in which the positive electrode was a graphite rod, and the negative electrode was con-

nected to the ITO glass substrate (Supplementary Section S2.1 for the electrochemical deposition system). The temperature of the growing electrolyte was controlled at 60 °C to ensure that the lactic acid works. The deposition time was fixed at 30 min to achieve high quality and uniformity. At the end of the film, the sample was washed with deionized water, and the surface moisture was removed with a high-pressure nitrogen gun for subsequent experiments.

2.1.3. Cu_2O Grinding

A plane grinder was widely used for the single-sided grinding and polishing of various materials, such as LED sapphire substrates, optical glass wafers, quartz wafers, silicon wafers, germanium wafers, molds, light guide plates, and optical skewer joints. The Cu_2O thin film was processed by grinding to smoothen the Cu_2O surface and facilitate the subsequent transfer of MoS_2 while maintaining the integrity of the morphological characteristics of MoS_2 and reducing the transfer failure rate. The rotation speed of the grinder was controlled at the minimum, and the time was set at 1 h. Considering Cu_2O was a thin film at the micrometer scale, we chose the micro grade at the scale of a diamond polishing sheet.

2.1.4. Experimental Materials and Drug Specifications of MoS_2

The substrate used to grow MoS_2 was silicon dioxide (SiO_2) for chemical vapor deposition (CVD; Supplementary Section S1.2 for obtaining MoS_2 layers). The thickness of the chosen silicon wafer (100) crystal plane was 300 nm. The purity of sulfur powder (S) and molybdenum oxide (MoO_3) powder was 99.98% and 99.95%, respectively, to avoid impurities that affect the CVD or the remaining impurities of grown single crystals. The quartz tubes and ceramic crucibles in the tubular thermal tubes were cleaned with aqua regia. The concentrations of nitric acid and hydrochloric acid were 37% and 68–69%, respectively, to avoid the adhesion of impurities from the previous growth during cleaning, which affects the experimental parameters and reproducibility of the next growth of monolayer MoS_2.

2.2. Process and Steps of CVD-Grown MoS_2

The majority of 2D material layer identification studies focus on film synthesis using mechanical stripping [48–50]. Most 2D material layer identification studies have focused on film synthesis through mechanical stripping [51]. In the present experiment, a 300 nm SiO_2 silicon substrate was prepared and cleaned with ultrasonic vibration in acetone for 10 min to remove impurities and oil stains on the surface; deionized water was then used to remove the organic solvent acetone (Supplementary Section S5 for CVD-grown MoS_2).

After 10 min, the sample was taken out, and the moisture on the surface of the ITO glass substrate was removed with a high-pressure nitrogen gun. The method used to grow MoS_2 was CVD [52–57]. The substrate was placed under specific pressure and temperature conditions and one or more precursors were chemically reacted on the surface of the substrate to produce a high-quality large-area thin film. The application of CVD in the preparation of single-layer TMDs starts with MoS_2 growth. The inert gas used to grow MoS_2 through CVD was argon. Afterward, 500 sccm of argon was used to clean the internal cavity and keep it in a clean environment. The heating rate was set to 20°C per min, the growth temperature was 650 °C, and the temperature was held for 30 min. Once the temperature was dropped to 400 °C, the lid was opened. The MoS_2 structure was obtained when the temperature decreases to room temperature. The experimental process was shown in Figure 1. With molybdenum trioxide (MoO_3) and sulfur powder (S) as precursors, a 2 cm × 2 cm silicon dioxide/silicon (SiO_2/Si) substrate was placed on the crucible and sent into the furnace tube. The vaporization point of MoO_3 was 650 °C [58–60]. The vaporization point of S was above 200 °C. Gas-phase MoO_3 undergoes two chemical reactions in high-temperature environments to produce molybdenum oxide (MoO_3-x) intermediates. The resulting molybdenum oxide intermediates diffuse to the substrate and vaporize to form a MoS_2 film. The distance between the two crucibles was 46 cm. This long

distance was to ensure that the vapor concentration gradient of sulfur was negligible on the substrate compared with that of the MoO_3 concentration gradient because the distance between MoO_3 and the substrate was small. CVD can effectively prepare single- and multi-layer MoS_2. It can grow high-quality single-crystal materials and prepare uniformly distributed thin films on a large area, which was conducive to subsequent optoelectronic component manufacturing.

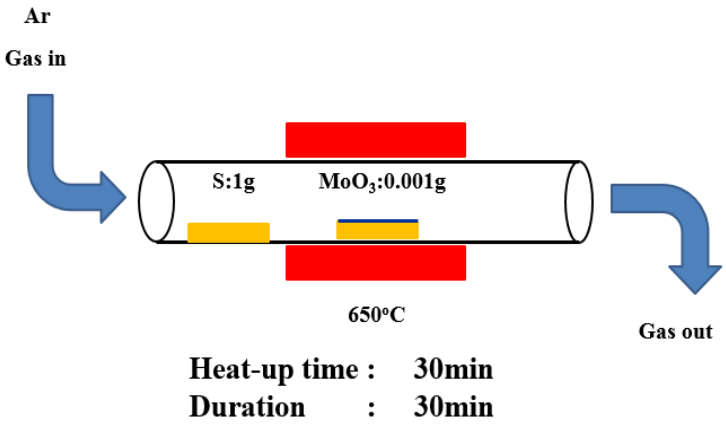

Figure 1. Schematic of a growing MoS_2 film.

MoS_2 Transfer Process

A spin coater was used to coat uniformly the photoresistant PMMA A5 on the substrate to transfer MoS_2 after CVD growth on the Cu_2O surface and left for the PMMA to dry. The substrate was covered with photoresistant liquid into 2 M NaOH as an etching solution for separating the substrate and PMMA A5. The removed photoresist was placed in DI water and blown dry with high-pressure nitrogen to prepare for the subsequent transfer. Then, PMMA A5 was placed on the original SiO_2 substrate, which was cut to an appropriate size with a three-axis leveling table and placed on the surface of the Cu_2O substrate. The temperature was set to 210° for about 30 s to make the PMMA adhere to the substrate. The sample was soaked in acetone for 30 min, and photoresistance was removed, leaving MoS_2 to complete the entire transfer process (Figure 2).

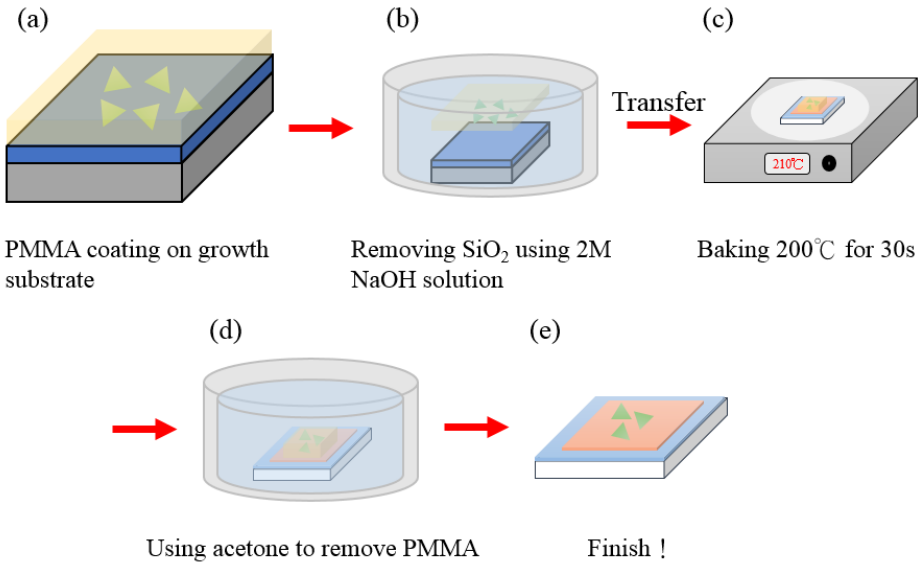

Figure 2. MoS_2 transfer flow chart: (**a**) PMMA coating on growth, (**b**) Removing SiO_2 using 2 M NaOH solution, (**c**) Baking 200 °C for 30 s, (**d**) Remove PMMA by acetone, (**e**) Complete the entire transfer process.

3. Results

3.1. Growth Results of MoS_2/Cu_2O

Based on the above growth methods and measurement results, the CVD-grown MoS_2 was transferred electrochemically to grown Cu_2O (Supplementary Section S4 for the results of Cu_2O electrochemical growth under different parameters). Material and optical characteristics were analyzed: Raman mapping (Supplementary Section S2.2 for micro-Raman Spectroscopy), SEM (Supplementary Section S2.5 for scanning electron microscope), and SHG measurements (Supplementary Section S2.8 for multiphoton excitation microscope).

3.1.1. Cu_2O Flattening Comparison

This study has used the Cu_2O film grown by the electrochemical method as the template for MoS_2 transfer. The SEM image is used to detect the success rate of the transfer, and the result is consistent with the Cu_2O image without transfer in the SEM image, as shown in Figure 3a,b. The reason for the failure is that the Cu_2O surface used for the electrochemical method is quite rough, and the rough surface causes the MoS_2 transfer to be broken or unable to be transferred because of the uneven surface. Afterward, the Cu_2O film was ground to smoothen the Cu_2O surface and facilitate the subsequent transfer of MoS_2 while maintaining the integrity of the morphological characteristics of MoS_2 and reducing the transfer failure rate. Figure 4a shows the AFM data results of Cu_2O before grinding. Under the following parameters, i.e., Z range of 740.16 nm, Rms of 97.496, and data scale of 0–800 nm (height), Figure 4b shows the results of Cu_2O after surface polishing by grinding. Under the following parameters, i.e., Z range of 94.623 nm, Rms of 3.849 nm, and data scale of 0–50 nm (height), the top and flat views of the Cu_2O film in the SEM image are shown in Figure 3c,d, respectively. The surface after grinding is smooth. According to the above data, grinding may be used to treat the Cu_2O surface.

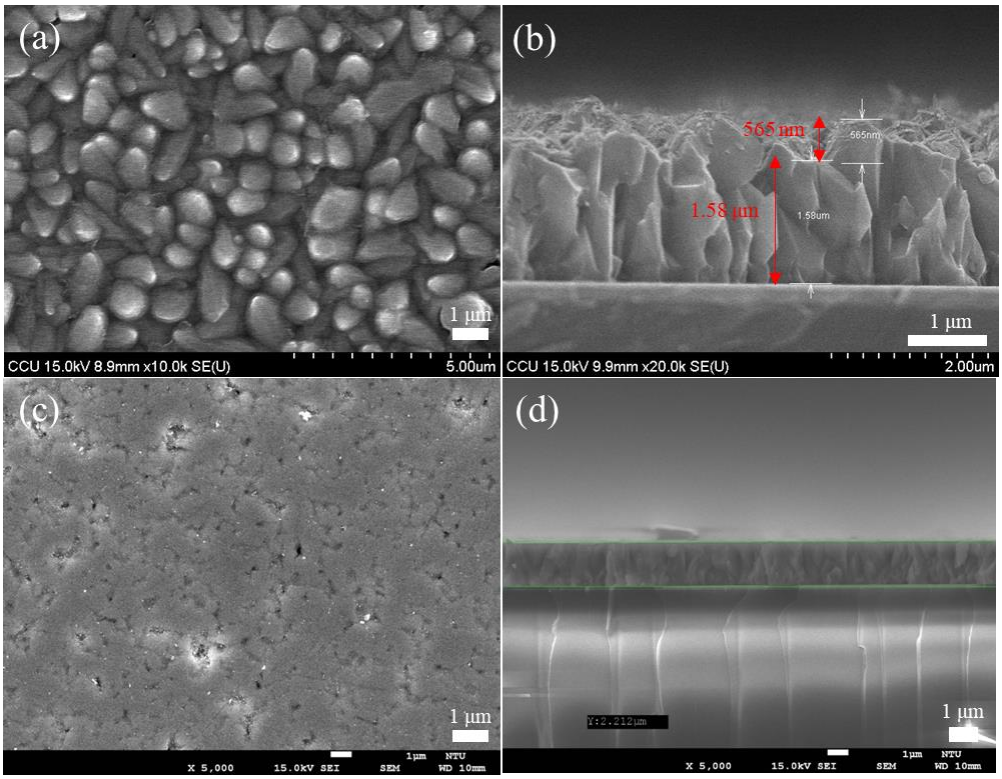

Figure 3. (**a**) Represents the front view of the Cu_2O film before polishing, (**b**) represent the side view of the Cu_2O film before polishing, (**c**) show the SEM images of the top view after Cu_2O polishing, (**d**) show the SEM images of the front view after Cu_2O polishing.

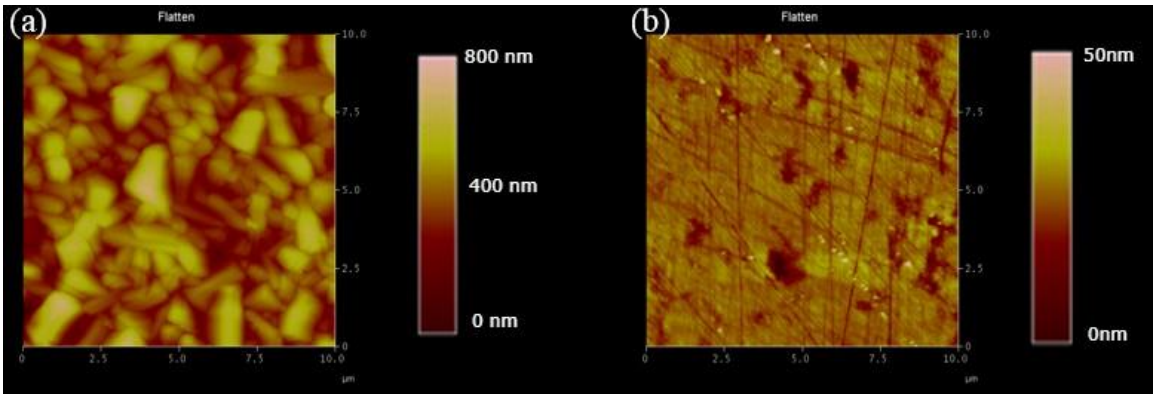

Figure 4. (**a**,**b**) AFM measurements of the Cu_2O film before and after polishing.

3.1.2. MoS_2 Transfer Result on Cu_2O

After the Cu_2O surface is polished by the abovementioned grinding method, the SEM image result shows that the surface is smoother than the original unpolished surface, and the surface roughness is reduced by 96% in the AFM measurement result (Supplementary Section S2.6 for atomic force microscope). Then CVD-grown MoS_2 film is transferred to the Cu_2O surface, and SEM is performed (Figure 5). Although few irregularities are observed on the surface of the Cu_2O, SEM analysis shows that MoS_2 is transferred successfully, and the morphological characteristics of MoS_2 are completely present on the surface of Cu_2O.

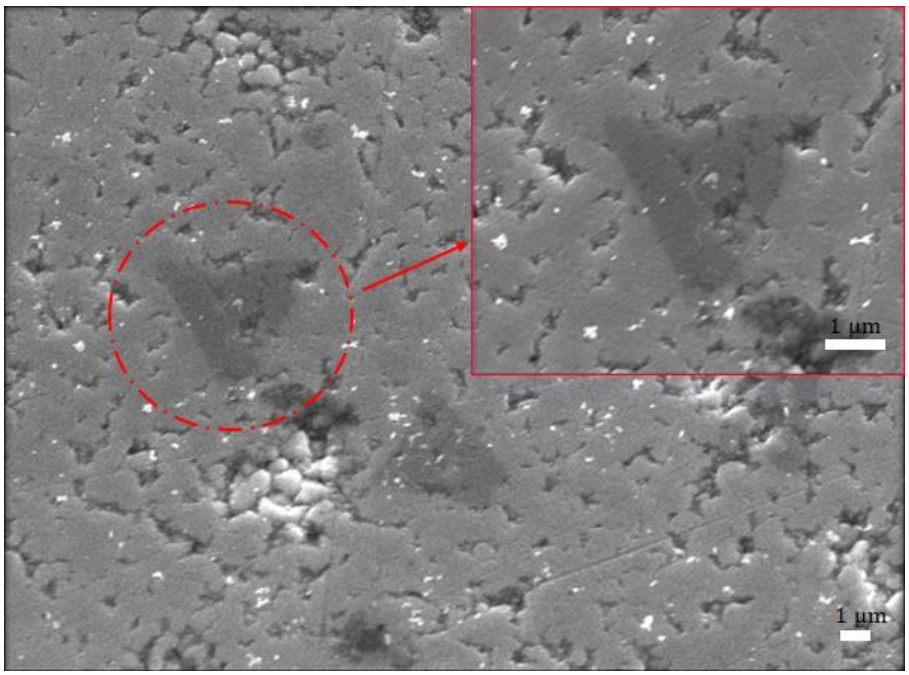

Figure 5. SEM image of MoS_2 transferred to the Cu_2O surface.

3.1.3. Analysis of MoS_2/Cu_2O Materials and Optical Properties

After the transfer of the CVD-grown MoS_2 film onto the electrochemically grown Cu_2O surface. Its material and optical properties are analyzed by employing OM (Supplementary Section S2.4 for optical microscope), SHG images, SEM, and Raman and PL mapping. A multiphoton image is used to identify the signal display during the MoS_2 transfer (Figure 6). The morphological characteristics of MoS_2 grown by CVD are obvious. A core point exists in most triangles, and when this core point corresponds to a multiphoton image, the signal becomes stronger than the color of the triangles other than the core point. Figure 6b

shows the multiphoton image of MoS_2/Cu_2O/ITO after the transfer. Although many blue irregularities in the image, they are not evenly dispersed to make it clear whether they are MoS_2 triangles.

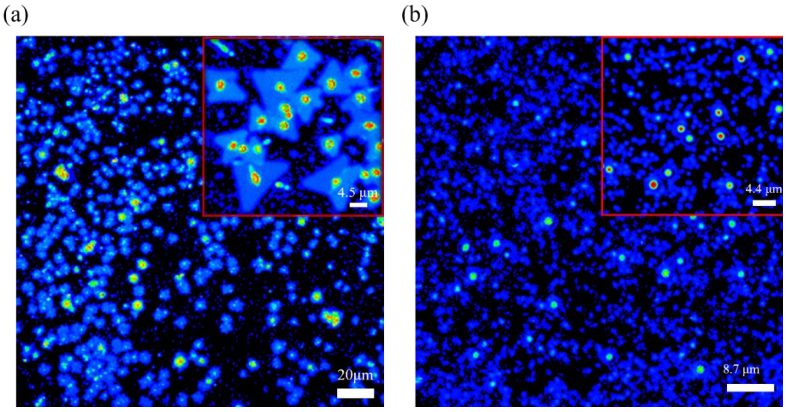

Figure 6. Multiphoton images of (**a**) $MoS_2/SiO_2/Si$ and of (**b**) MoS_2/Cu_2O/ITO.

However, the comparison of the obvious bright spots in the image in Figure 6a suggests that a bright spot signal may be the core image after MoS_2 transfer and because Cu_2O is not completely flat like the SiO_2 surface after being polished. Moreover, this bright spot at the center of MoS_2 is due to the nucleation of MoS_2. The growth parameters, such as carrier gas, growth temperature, precursors, substrates, and promoters can affect the nucleation and growth modes of MoS_2 [61]. However, Ho Kwon Kim et al. has shown that the pre-exposure of growth substrates to alkali metal halides and the Mo precursor before the growth stage appears can suppress nucleation of MoS_2 [62]. Therefore, the other blue part may be a multi-photon image of a mixture of MoS_2 and Cu_2O. As shown in Figure 5, the grown MoS_2 has been successfully transferred to the Cu_2O film. These two data can be combined, proving that MoS_2 has been successfully transferred to the Cu_2O film by grinding and transfer. Raman mapping, which is the best method to analyze the number of layers, has been used to analyze the image of the transferred MoS_2/Cu_2O sample [63–65]. In this study, a 532 nm band is used as a laser excitation light source. From Figure 7b we can observe that the blue-green area is the MoS_2 film, and the red area is part of a Cu_2O film. The 532 nm band was used as the laser excitation light source in this study. As shown in Figure 7a, the Raman shift of MoS_2 has a peak at 384.3 before transfer while the Raman shift had a peak at 402.8 cm^{-1} after the transfer. The Raman shift of Cu_2O before the transfer has a peak at 221.8 cm^{-1}. After transferring MoS_2 onto the Cu_2O film, the Raman shift did reach peaks at 221.8, 384.3, and 402.8 cm^{-1}. It can be clearly inferred that the Raman peak of Cu_2O appearing at 221.8 cm^{-1} indicates that the surface of Cu_2O was partially oxidized. Similarly, the Raman shifts of MoS_2 at 384.3 and 402.8 cm^{-1} are in accordance with E_{12g} and A_{1g}, respectively, and combined vibrations of two different phonons ($A_{1g}(M)-LA(M)$), respectively, which indicates the existence of MoS_2 structures [66–69]. In the Cu_2O/MoS_2 composite films, the diffraction peaks of Cu_2O and MoS_2 are still observed. The result shows that the grown MoS_2 has a uniform film in the image and can replace the morphology. E_{12g} and A_{1g} vibration modes are the main signals for the judgment of MoS_2. The two vibration modes are highly dependent on the thickness of MoS_2. When the Δk value of the subtraction of E_{12g} and A_{1g} peaks is less than 20 cm^{-1}, the analyzed MoS_2 is regarded as a single-layer structure.

Figure 8a shows the OM image of MoS_2/Cu_2O, Figure 8b illustrates the 625-band image selected for the PL mapping image. The MoS_2 spectrum consists of two peaks corresponding to the A1 and B1 excitons at 667 nm (1.86 eV) and 627 nm (1.97 eV), respectively. The measured PL for Cu_2O grown by the electrochemical method was about 720–900 nm. In the measurement of the PN heterostructure material combination of MoS_2/Cu_2O, Raman measurement was first performed on the OM image. After the signal of MoS_2 is found, PL

measurement is carried out, and the combined structure is examined through the measurement results to show that the band range covers 625–900 nm. We found that a micro signal is generated at about 627 nm in the orange elliptical dashed circle, and the wavelength of 627 nm belongs to the B2 excitons of MoS_2. The signal gradually increases when it approaches 670 nm. However, the Cu_2O signal is not in this part because its light-emitting band starts to generate signals from 720 nm. Therefore, the Cu_2O film may be too thick, and the single-layer MoS_2 film thickness is only 0.7 nm, so the two heterostructure materials are combined in the wavelength range of 670–700 nm. The entire signal undergoes a red-shifted phenomenon because the Cu_2O film signal is strong.

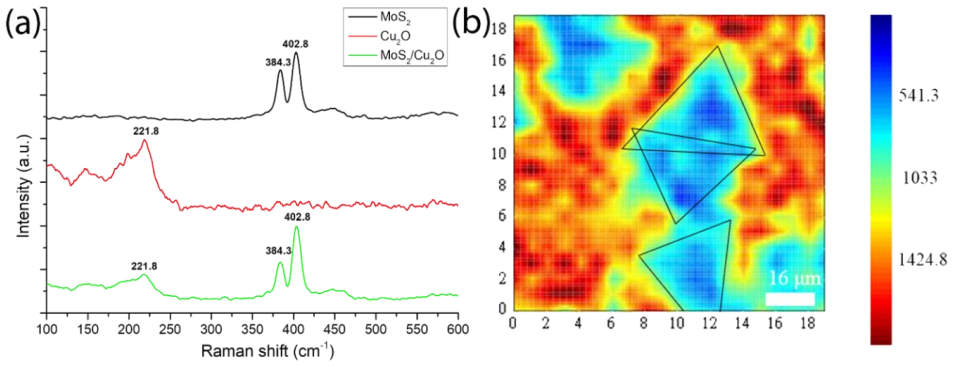

Figure 7. (**a**) Raman spectrum after MoS_2 transfer to Cu_2O surface and (**b**) Raman mapping of MoS_2/Cu_2O.

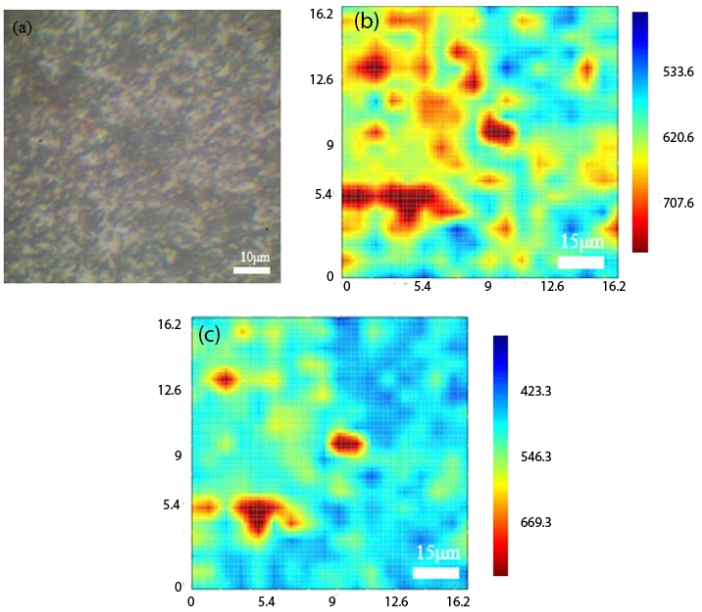

Figure 8. (**a**) OM image of MoS_2/Cu_2O, (**b**) 625 band for PL mapping image, (**c**) 675 band for PL mapping image.

3.2. Photocurrent Response Analysis

This research uses the preparation of biosensors, and the photocurrent measurement system and impedance analysis system set up in the laboratory (see Supplement 1, Section S6 for Analysis of Structural Characteristics of Photoelectrochemical Biosensors). The photocurrent measurement of the three lung cancer cells A549, H460 and H520 was carried out by the carrier transport mechanism of photogenerated charge, and the zigzags-toothed microelectrode was used to perform aggregation and impedance analysis of the cancer cells. In this study, we utilized two characteristic substances, glutathione (GSH) and glutathione disulfide (GSSG), to verify the detection mechanism of the developed

biosensor. Generally, GSH in cells exists in two forms: 90% of GSH is present in the cytoplasm as reduced GSH, and 10% is present in the mitochondria. For healthy cells, the ratio of GSH to GSSG is greater than 10:1. However, when cells become cancerous, the ratio of GSH to GSSG decreases [70,71]. Because the majority carriers in N-type PEC are electrons and hence GSSG participating in PEC reaction is more significant. When irradiated, electron-hole pairs are generated, GSSG recombines with photo-generated electrons, and photo-generated holes are detected, forming a system of hole currents. As the degree of canceration becomes more severe, the concentration of GSSG contained in cancer cells increases, and the measured photocurrent also increases [72,73]. On the contrary, the majority of carriers in the P-type PEC biosensor are holes and hence GSH participates in the PEC reaction more significantly. After being illuminated, GSH recombines with photo-generated holes, photo-generated electrons are detected, and a system of electron flow is formed. The more severe the carcinogenesis of the structure, the smaller the GSH concentration and also a decrease of the photocurrent [74,75]. As shown in Figure 9 the photocurrent decreased with the increase of suspended cell density, which indicated that more GSH was involved in the PEC process. From Figure 10, it can be known that different cells have different amounts of change, there is a highly linear relationship between the photocurrent change and the number of cells, and the linear regression of the three cell types is as high as 99%. The slopes corresponding to the three cell lines A549, NCI-H460 and NCI-H520 were approximately 0.000452, 0.000749 and 0.000174, respectively. By measuring the magnitude of the photocurrent, we can calculate the regression curve equation, thereby identifying which cell of the three cells is. In the growth mechanism of Cu_2O, as the thickness increases, the stress or dislocation will increase, resulting in a certain optimal thickness of the material. Previous studies also shows that the best growth thickness of Cu_2O under the environment and parameters of our growth is 2 μm [76].

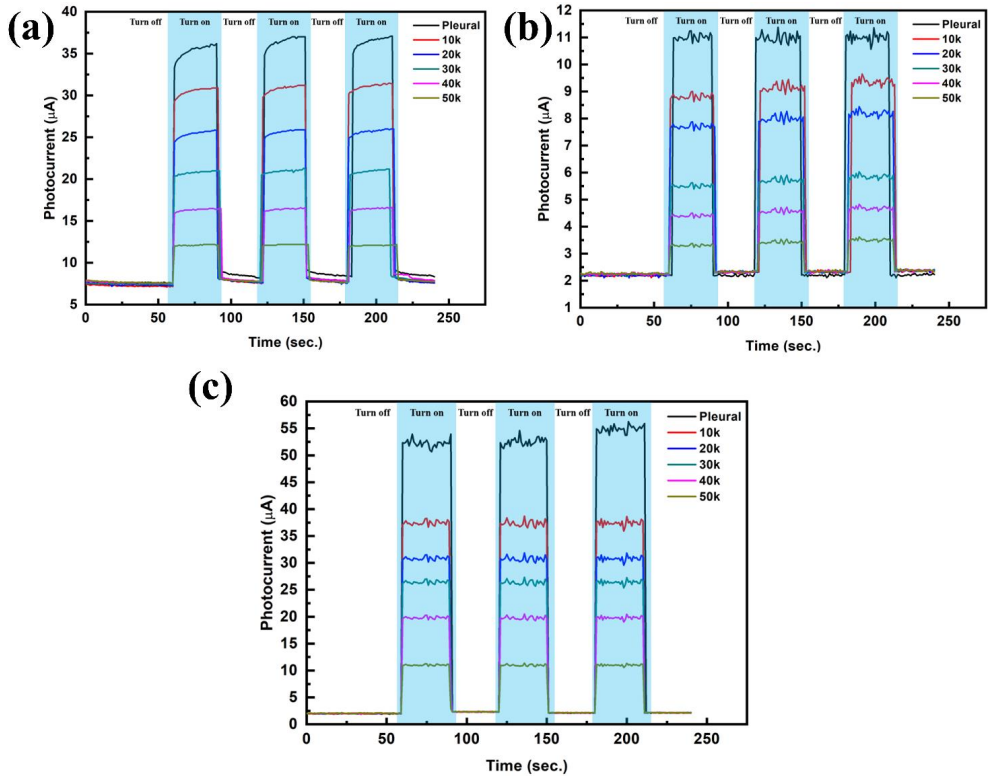

Figure 9. P. (**a**) Photocurrent responses of A549 under different cell numbers, (**b**) Photocurrent responses of NCI-H460 under different cell numbers and (**c**) Photocurrent responses of NCI-H520 under different cell numbers.

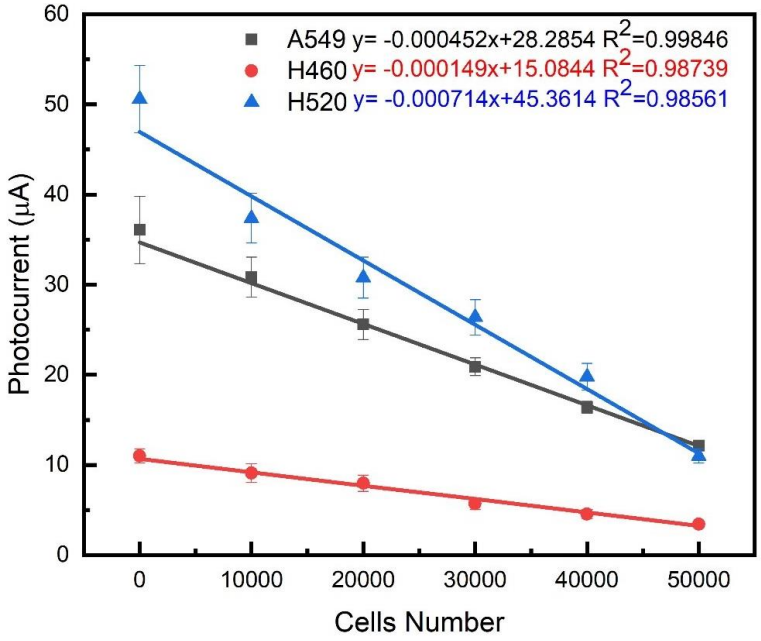

Figure 10. Linear relationship between photocurrent changes and cell number in three lung cancer cell lines on biosensing chips.

4. Discussion

When the MoS_2 film has a single-layer structure, the A_{1g} signal is stronger than that of a multilayer film. If the MoS_2 film has a multilayer structure, the E_{12g} signal is stronger than that of a single-layer film. The PL signal of MoS_2 also decreases as the number of layers increases. Therefore, we can observe the contrast of the image by selecting the PL mapping images of 625 and 675 nm, corresponding to the color bar value. Single- and multi-layer MoS_2 film signals are found in the selected 625-band image compared with much fewer signals in the 675-band image. When we grow the MoS_2 film, single- and multi-layer structures form. In the selection of images for mapping, more multi-layer MoS_2 films are covered. The PL measurement results in this study use a 532 nm laser as the excitation light source to measure the PL of a single-layer MoS_2 film. The measurement results show that a strong signal is generated at the wavelength of 667 nm, and the energy is 1.84 eV after conversion. It is the energy gap of single-layer MoS_2. However, from Gang Li et al., the energy band alignment of bulk MoS_2 and single layer MoS_2 was observed at 1.4 eV and 1.78 eV, respectively [29]. From our study, the single layer MoS_2 was observed at 1.84 eV, close to the previous observations. The future scope of this project can be split into two aspects. First, after the two materials are combined, by using them as electric double-layer transistors their electrical properties can be tested. After confirming the positive state of the oxide trap. We can also try to bombard the element with high-energy particles to explore its characteristic influence and figure out if it affects the transformation of the mechanism. If the result of the electron beam bombardment affects the element and causes the characteristics to change, it can be checked again whether the electrical property changes from the positive oxide trap state to the negative interface trap state. Second, CVD can be performed to grow MoS_2 in the 2H phase. MoS_2 has three crystal structures: 2H (semiconductor characteristics), 1T (metallic characteristics), and 3R (semiconductor characteristics). The intensity difference can be detected in the PL mapping and electrostatic force microscope (EFM) images of 2H-MoS_2 and 1T-MoS_2. The future scope of this study is to collect a large amount of data to build a large-scale database by measuring the cell impedance and photocurrent in the patient's pleural effusion. After analyzing the data through Artificial Intelligence (AI), a human-machine display interface will be designed which provides the types of cancer cells defined by the system, assisting physicians to determine the patient's cancer status and provide appropriate treatment methods.

5. Conclusions

In this study, an electrochemical method was used to grow a Cu_2O film with a uniform and superior crystal lattice. The micro-roughened surface structure of Cu_2O was polished by grinding. Then, CVD-grown single crystal MoS_2 was transferred to the Cu_2O film. OM, SHG, SEM, Raman, and PL mapping measurements were used to analyze the combination of the two materials. Electrochemical methods were successfully used to achieve relatively good electrical properties. TEM showed that Cu_2O is a single crystal structure, and SEM revealed that the surface should be processed by subsequent grinding methods. After grinding and polishing were performed, AFM and SEM were used to obtain the experimental results. MoS_2 structure was grown through CVD, and E_{12g} and A_{1g} peaks were obtained via Raman analysis. The main luminescence peak at 667 nm was determined through PL analysis. The single layer of MoS_2 was transferred to the polished Cu_2O surface, which was confirmed by SEM and SHG results. Raman and PL mapping image analysis on MoS_2/Cu_2O indicated that the grown MoS_2 had a uniform film. The combined structure was measured through PL measurement to verify that the band range covered 625–900 nm. A micro signal was found at the 627 nm wavelength. It belonged to the B2 excitons of MoS_2 and tended to increase gradually as it approached 670 nm. The Cu_2O film was too thick, whereas the thickness of the single-layer MoS_2 film was only 0.7 nm. As such, the two heterostructure materials combined in the wavelength range of 670–700 nm. The strong signal of the Cu_2O film itself led to a red shift in the entire signal. This study also successfully fabricated a low-cost PEC biosensor that is highly sensitive to lung cancer cells which is a rapid way to detect lung cancer cell types in hydroplegia. The photocurrent response is measured using the MoS_2/Cu_2O biochip material grown by electrochemical deposition. As the number of cancer cells measured increases, the content of oxidized GSSG also increases, and the measured photocurrent decreases accordingly. It is also possible to use dielectrophoresis to gather cancer cells to form a pearl string, measure unlabeled cancer cells, and use the slope of the admittance value to shape lung cancer cells. The linear regression curve is compared with the admittance value and the photocurrent measurement value to distinguish the types of cancer cells in the pleural effusion.

Supplementary Materials: The following supporting information can be downloaded at: https://www.mdpi.com/article/10.3390/ijms23094745/s1.

Author Contributions: Conceptualization, V.E.F., S.-W.F. and. S.B.A.; methodology, S.-W.F., Y.-M.T., Y.-C.H. and Y.-S.L.; software, S.-W.F., V.E.F. and Y.-S.L.; validation, S.B.A., S.-W.F. and H.-C.W.; formal analysis, S.-W.F., Y.-M.T. and Y.-S.L.; investigation, Y.-S.L., Y.-H.W. and A.M.; resources, S.-W.F., Y.-M.T., Y.-C.H. and Y.-H.W.; data curation, S.B.A.; writing—original draft preparation, S.B.A., A.M. and Y.-H.W.; writing—review and editing, A.M. and H.-C.W.; supervision, S.-W.F., V.E.F. and H.-C.W.; and project administration, H.-C.W. All authors have read and agreed to the published version of the manuscript.

Funding: This research was supported by the Ministry of Science and Technology, The Republic of China under the grants MOST 105-2923-E-194-003 MY3, 108-2823-8-194-002, 109-2622-8-194-001-TE1, and 109-2622-8-194-007. This work was financially/partially supported by the Advanced Institute of Manufacturing with High-tech Innovations (AIM-HI) and the Center for Innovative Research on Aging Society (CIRAS) from The Featured Areas Research Center Program within the framework of the Higher Education Sprout Project by the Ministry of Education (MOE) and Kaohsiung Armed Forces General Hospital research project 108-016 in Taiwan.

Institutional Review Board Statement: Not Applicable.

Informed Consent Statement: Not Applicable.

Data Availability Statement: Not Applicable.

Conflicts of Interest: The authors declare no conflict of interest.

References

1. Geim, A.K.; Novoselov, K.S. The rise of graphene. In *Nanoscience and Technology: A Collection of Reviews from Nature Journals*; World Scientific: Singapore, 2010; pp. 11–19.
2. Sarma, S.D.; Adam, S.; Hwang, E.H.; Rossi, E. Electronic transport in two-dimensional graphene. *Rev. Mod. Phys.* **2011**, *83*, 407. [CrossRef]
3. Lin, X.; Su, L.; Si, Z.; Zhang, Y.; Bournel, A.; Zhang, Y.; Klein, J.-O.; Fert, A.; Zhao, W. Gate-Driven Pure Spin Current in Graphene. *Phys. Rev. Appl.* **2017**, *8*, 034006. [CrossRef]
4. Wu, C.; Zhang, J.; Tong, X.; Yu, P.; Xu, J.; Wu, J.; Wang, Z.M.; Lou, J.; Chueh, Y.-L. A critical review on enhancement of photocatalytic hydrogen production by molybdenum disulfide: From growth to interfacial activities. *Small* **2019**, *15*, 1900578. [CrossRef] [PubMed]
5. Yang, D.; Wang, H.; Luo, S.; Wang, C.; Zhang, S.; Guo, S. Paper-Cut Flexible Multifunctional Electronics Using MoS2 Nanosheet. *Nanomaterials* **2019**, *9*, 922. [CrossRef] [PubMed]
6. Zhang, Y.; Wan, Q.; Yang, N. Recent Advances of Porous Graphene: Synthesis, Functionalization, and Electrochemical Applications. *Small* **2019**, *15*, e1903780. [CrossRef] [PubMed]
7. Choi, M.S.; Lee, G.-H.; Yu, Y.-J.; Lee, D.-Y.; Lee, S.H.; Kim, P.; Hone, J.; Yoo, W.J. Controlled charge trapping by molybdenum disulphide and graphene in ultrathin heterostructured memory devices. *Nat. Commun.* **2013**, *4*, 1624. [CrossRef] [PubMed]
8. Han, T.; Liu, H.; Wang, S.; Chen, S.; Xie, H.; Yang, K. Probing the Field-Effect Transistor with Monolayer MoS2 Prepared by APCVD. *Nanomaterials* **2019**, *9*, 1209. [CrossRef] [PubMed]
9. Lee, C.-H.; Lee, G.-H.; van der Zande, A.M.; Chen, W.; Li, Y.; Han, M.; Cui, X.; Arefe, G.; Nuckolls, C.; Heinz, T.F.; et al. Atomically thin p–n junctions with van der Waals heterointerfaces. *Nat. Nanotechnol.* **2014**, *9*, 676–681. [CrossRef]
10. Lu, G.Z.; Wu, M.-J.; Lin, T.-N.; Chang, C.-Y.; Lin, W.-L.; Chen, Y.T.; Hou, C.-F.; Cheng, H.-J.; Lin, T.-Y.; Shen, J.-L.; et al. Electrically Pumped White-Light-Emitting Diodes Based on Histidine-Doped MoS_2 Quantum Dots. *Small* **2019**, *15*, 1901908. [CrossRef]
11. Park, Y.J.; Sharma, B.K.; Shinde, S.M.; Kim, M.-S.; Jang, B.; Kim, J.-H.; Ahn, J.-H. All MoS_2-Based Large Area, Skin-Attachable Active-Matrix Tactile Sensor. *ACS Nano* **2019**, *13*, 3023–3030. [CrossRef]
12. Radisavljevic, B.; Radenovic, A.; Brivio, J.; Giacometti, V.; Kis, A. Single-layer MoS_2 transistors. *Nat. Nanotechnol.* **2011**, *6*, 147–150. [CrossRef]
13. Roh, J.; Ryu, J.H.; Baek, G.W.; Jung, H.; Seo, S.G.; An, K.; Jeong, B.G.; Lee, D.C.; Hong, B.H.; Bae, W.K.; et al. Threshold Voltage Control of Multilayered MoS2 Field-Effect Transistors via Octadecyltrichlorosilane and their Applications to Active Matrixed Quantum Dot Displays Driven by Enhancement-Mode Logic Gates. *Small* **2019**, *15*, 1803852. [CrossRef] [PubMed]
14. Zhao, J.; Li, N.; Yu, H.; Wei, Z.; Liao, M.; Chen, P.; Wang, S.; Shi, D.; Sun, Q.; Zhang, G. Highly Sensitive MoS_2 Humidity Sensors Array for Noncontact Sensation. *Adv. Mater.* **2017**, 29. [CrossRef] [PubMed]
15. Zhang, P.; Yang, S.; Pineda-Gómez, R.; Ibarlucea, B.; Ma, J.; Lohe, M.R.; Akbar, T.F.; Baraban, L.; Cuniberti, G.; Feng, X.; et al. Electrochemically Exfoliated High-Quality 2H-MoS_2 for Multiflake Thin Film Flexible Biosensors. *Small* **2019**, *15*, 1901265. [CrossRef]
16. Yang, K.; Liu, H.; Wang, S.; Li, W.; Han, T. A Horizontal-Gate Monolayer MoS2 Transistor Based on Image Force Barrier Reduction. *Nanomaterials* **2019**, *9*, 1245. [CrossRef] [PubMed]
17. Yadav, V.; Roy, S.; Singh, P.; Khan, Z.; Jaiswal, A. 2D MoS2-based nanomaterials for therapeutic, bioimaging, and biosensing applications. *Small* **2019**, *15*, 1803706. [CrossRef] [PubMed]
18. Shin, M.; Yoon, J.; Yi, C.; Lee, T.; Choi, J.-W. Flexible HIV-1 Biosensor Based on the Au/MoS2 Nanoparticles/Au Nanolayer on the PET Substrate. *Nanomaterials* **2019**, *9*, 1076. [CrossRef] [PubMed]
19. Sarkar, D.; Liu, W.; Xie, X.; Anselmo, A.C.; Mitragotri, S.; Banerjee, K. MoS_2 Field-Effect Transistor for Next-Generation Label-Free Biosensors. *ACS Nano* **2014**, *8*, 3992–4003. [CrossRef]
20. Jia, X.; Huang, J.; Li, Y.; Yang, J.; Song, H. Monodisperse Cu nanoparticles @ MoS_2 nanosheets as a lubricant additive for improved tribological properties. *Appl. Surf. Sci.* **2019**, *494*, 430–439. [CrossRef]
21. Zhao, Y.-F.; Yang, Z.-Y.; Zhang, Y.-X.; Jing, L.; Guo, X.; Ke, Z.; Hu, P.; Wang, G.; Yan, Y.-M.; Sun, K.-N. Cu_2O Decorated with Cocatalyst MoS_2 for Solar Hydrogen Production with Enhanced Efficiency under Visible Light. *J. Phys. Chem. C* **2014**, *118*, 14238–14245. [CrossRef]
22. Paracchino, A.; Laporte, V.; Sivula, K.; Grätzel, M.; Thimsen, E. Highly active oxide photocathode for photoelectrochemical water reduction. *Nat. Mater.* **2011**, *10*, 456–461. [CrossRef]
23. Mahmoud, M.A.; Qian, W.; El-Sayed, M.A. Following Charge Separation on the Nanoscale in Cu_2O–Au Nanoframe Hollow Nanoparticles. *Nano Lett.* **2011**, *11*, 3285–3289. [CrossRef]
24. Radi, A.; Pradhan, D.; Sohn, Y.; Leung, K.T. Nanoscale shape and size control of cubic, cuboctahedral, and octahedral $Cu-Cu_2O$ core−shell nanoparticles on Si (100) by one-step, templateless, capping-agent-free electrodeposition. *ACS Nano* **2010**, *4*, 1553–1560. [CrossRef]
25. De Jongh, P.E.; Vanmaekelbergh, D.; Kelly, J.J. Photoelectrochemistry of Electrodeposited Cu_2O. *J. Electrochem. Soc.* **2000**, *147*, 486–489. [CrossRef]
26. Li, Z.; Ezhilarasu, G.; Chatzakis, I.; Dhall, R.; Chen, C.-C.; Cronin, S.B. Indirect Band Gap Emission by Hot Electron Injection in Metal/MoS_2 and Metal/WSe_2 Heterojunctions. *Nano Lett.* **2015**, *15*, 3977–3982. [CrossRef]

27. Zhao, X.; Li, Y.; Guo, Y.; Chen, Y.; Su, Z.; Zhang, P. Coral-like MoS_2/Cu_2O porous nanohybrid with dual-electrocatalyst performances. *Adv. Mater. Interfaces* **2016**, *3*, 1600658. [CrossRef]
28. Mukundan, A.; Tsao, Y.-M.; Artemkina, S.B.; Fedorov, V.E.; Wang, H.-C. Growth Mechanism of Periodic-Structured MoS_2 by Transmission Electron Microscopy. *Nanomaterials* **2021**, *12*, 135. [CrossRef]
29. Fang, L.; Wang, F.; Chen, Z.; Qiu, Y.; Zhai, T.; Hu, M.; Zhang, C.; Huang, K. Flower-like MoS_2 decorated with Cu_2O nanoparticles for non-enzymatic amperometric sensing of glucose. *Talanta* **2017**, *167*, 593–599. [CrossRef]
30. Li, G.; Zhang, W.; Hou, J.; Li, T.; Li, P.; Wang, Y.; Liu, J.; Wang, K. Enhanced visible light photochemical activity and stability of MoS_2/Cu_2O nanocomposites by tunable heterojunction. *Mater. Today Commun.* **2020**, *23*, 100933. [CrossRef]
31. Koyun, O.; Sahin, Y. Voltammetric determination of nitrite with gold nanoparticles/poly (methylene blue)-modified pencil graphite electrode: Application in food and water samples. *Ionics* **2018**, *24*, 3187–3197. [CrossRef]
32. Amini, N.; Gholivand, M.B.; Shamsipur, M.; Movahedi, A.A.M.; Farahi, S.; Habibi-Rezaei, M.; Maleki, A.; Rezaee, M.; Naderi, K. Fabrication of a glycation induced amyloid nanofibril and polyalizarin yellow R nanobiocomposite: Application for electrocatalytic determination of hydrogen peroxide. *Int. J. Biol. Macromol.* **2018**, *123*, 1297–1304. [CrossRef] [PubMed]
33. Agrisuelas, J.; González-Sánchez, M.-I.; Gómez-Monedero, B.; Valero, E. A Comparative Study of Poly(Azure A) Film-Modified Disposable Electrodes for Electrocatalytic Oxidation of H_2O_2: Effect of Doping Anion. *Polymers* **2018**, *10*, 48. [CrossRef] [PubMed]
34. Liu, Y.; Song, N.; Ma, Z.; Zhou, K.; Gan, Z.; Gao, Y.; Tang, S.; Chen, C. Synthesis of a poly (N-methylthionine)/reduced graphene oxide nanocomposite for the detection of hydroquinone. *Mater. Chem. Phys.* **2019**, *223*, 548–556. [CrossRef]
35. da Silva, W.; Ghica, M.E.; Brett, C.M. Novel nanocomposite film modified electrode based on poly (brilliant cresyl blue)-deep eutectic solvent/carbon nanotubes and its biosensing applications. *Electrochim. Acta* **2019**, *317*, 766–777. [CrossRef]
36. Shamspur, T.; Biniaz, Z.; Mostafavi, A.; Torkzadeh-Mahani, M.; Mohamadi, M. An Electrochemical Immunosensor Based on Poly(Thionine)-Modified Carbon Paste Electrode for the Determination of Prostate Specific Antigen. *IEEE Sens. J.* **2018**, *18*, 4861–4868. [CrossRef]
37. Ali, S.; Gupta, A.; Shafiei, M.; Langford, S. Recent Advances in Perylene Diimide-Based Active Materials in Electrical Mode Gas Sensing. *Chemosensors* **2021**, *9*, 30. [CrossRef]
38. Kozitsina, A.N.; Svalova, T.S.; Malysheva, N.N.; Okhokhonin, A.V.; Vidrevich, M.B.; Brainina, K.Z. Sensors Based on Bio and Biomimetic Receptors in Medical Diagnostic, Environment, and Food Analysis. *Biosensors* **2018**, *8*, 35. [CrossRef]
39. Feng, T.; Chen, X.; Qiao, X.; Sun, Z.; Wang, H.; Qi, Y.; Hong, C. Graphene oxide supported rhombic dodecahedral Cu_2O nanocrystals for the detection of carcinoembryonic antigen. *Anal. Biochem.* **2015**, *494*, 101–107. [CrossRef]
40. Ma, H.; Li, Y.; Wang, Y.; Hu, L.; Zhang, Y.; Fan, D.; Yan, T.; Wei, Q. Cubic Cu_2O nanoframes with a unique edge-truncated structure and a good electrocatalytic activity for immunosensor application. *Biosens. Bioelectron.* **2016**, *78*, 167–173. [CrossRef]
41. Park, J.C.; Kim, J.; Kwon, H.; Song, H. Gram-Scale Synthesis of Cu_2O Nanocubes and Subsequent Oxidation to CuO Hollow Nanostructures for Lithium-Ion Battery Anode Materials. *Adv. Mater.* **2009**, *21*, 803–807. [CrossRef]
42. Wang, H.; Zhang, Y.; Wang, Y.; Ma, H.; Du, B.; Wei, Q. Facile synthesis of cuprous oxide nanowires decorated graphene oxide nanosheets nanocomposites and its application in label-free electrochemical immunosensor. *Biosens. Bioelectron.* **2017**, *87*, 745–751. [CrossRef]
43. Su, S.; Sun, H.; Cao, W.; Chao, J.; Peng, H.; Zuo, X.; Yuwen, L.; Fan, C.; Wang, L. Dual-Target Electrochemical Biosensing Based on DNA Structural Switching on Gold Nanoparticle-Decorated MoS_2 Nanosheets. *ACS Appl. Mater. Interfaces* **2016**, *8*, 6826–6833. [CrossRef]
44. Su, S.; Zou, M.; Zhao, H.; Yuan, C.; Xu, Y.; Zhang, C.; Wang, L.; Fan, C.; Wang, L. Shape-controlled gold nanoparticles supported on MoS_2 nanosheets: Synergistic effect of thionine and MoS_2 and their application for electrochemical label-free immunosensing. *Nanoscale* **2015**, *7*, 19129–19135. [CrossRef]
45. Wang, X.; Shen, L.; Deng, W.; Yan, M.; Liu, H.; Ge, S.; Yu, J.; Song, X. A sensitive electrochemiluminescent immunosensor based on 3D-flower-like MoS_2 microspheres and using AuPt nanoparticles for signal amplification. *RSC Adv.* **2016**, *6*, 23411–23419. [CrossRef]
46. Wu, I.-C.; Weng, Y.-H.; Lu, M.-Y.; Jen, C.-P.; Fedorov, V.E.; Chen, W.C.; Wu, M.T.; Kuo, C.-T.; Wang, H.-C. Nano-structure ZnO/Cu_2O photoelectrochemical and self-powered biosensor for esophageal cancer cell detection. *Opt. Express* **2017**, *25*, 7689–7706. [CrossRef]
47. Chen, Y.-S.; Liao, C.-H.; Chueh, Y.-L.; Lai, C.-C.; Chen, L.-Y.; Chu, A.-K.; Kuo, C.-T.; Wang, H.-C. High performance Cu_2O/ZnO core-shell nanorod arrays synthesized using a nanoimprint GaN template by the hydrothermal growth technique. *Opt. Mater. Express* **2014**, *4*, 1473–1486. [CrossRef]
48. Zhao, Y.; Luo, X.; Li, H.; Zhang, J. Interlayer breathing and shear modes in few-trilayer MoS_2 and WSe_2. *Nano Lett.* **2013**, *13*, 1007–1015. [CrossRef]
49. Li, H.; Wu, J.; Yin, Z.; Zhang, H. Preparation and Applications of Mechanically Exfoliated Single-Layer and Multilayer MoS_2 and WSe_2 Nanosheets. *Acc. Chem. Res.* **2014**, *47*, 1067–1075. [CrossRef]
50. Li, H.; Lu, G.; Yin, Z.; He, Q.; Li, H.; Zhang, Q.; Zhang, H. Optical identification of single-and few-layer MoS_2 sheets. *Small* **2012**, *8*, 682–686. [CrossRef]
51. Li, K.-C.; Lu, M.-Y.; Nguyen, H.T.; Feng, S.-W.; Artemkina, S.B.; Fedorov, V.E.; Wang, H.-C. Intelligent Identification of MoS_2 Nanostructures with Hyperspectral Imaging by 3D-CNN. *Nanomaterials* **2020**, *10*, 1161. [CrossRef]

52. Wang, Q.; Lei, Y.; Wang, Y.; Liu, Y.; Song, C.; Zeng, J.; Song, Y.; Duan, X.; Wang, D.; Li, Y. Atomic-scale engineering of chemical-vapor-deposition-grown 2D transition metal dichalcogenides for electrocatalysis. *Energy Environ. Sci.* **2020**, *13*, 1593–1616. [CrossRef]
53. Cai, Z.; Liu, B.; Zou, X.; Cheng, H.-M. Chemical Vapor Deposition Growth and Applications of Two-Dimensional Materials and Their Heterostructures. *Chem. Rev.* **2018**, *118*, 6091–6133. [CrossRef] [PubMed]
54. Jeon, J.; Jang, S.K.; Jeon, S.M.; Yoo, G.; Jang, Y.H.; Park, J.-H.; Lee, S. Layer-controlled CVD growth of large-area two-dimensional MoS_2 films. *Nanoscale* **2014**, *7*, 1688–1695. [CrossRef] [PubMed]
55. Lee, Y.-H.; Zhang, X.-Q.; Zhang, W.; Chang, M.-T.; Lin, C.-T.; Chang, K.-D.; Yu, Y.-C.; Wang, J.T.-W.; Chang, C.-S.; Li, L.-J.; et al. Synthesis of Large-Area MoS_2 Atomic Layers with Chemical Vapor Deposition. *Adv. Mater.* **2012**, *24*, 2320–2325. [CrossRef]
56. van der Zande, A.M.; Huang, P.Y.; Chenet, D.A.; Berkelbach, T.C.; You, Y.; Lee, G.-H.; Heinz, T.F.; Reichman, D.R.; Muller, D.A.; Hone, J.C. Grains and grain boundaries in highly crystalline monolayer molybdenum disulphide. *Nat. Mater.* **2013**, *12*, 554–561. [CrossRef]
57. Najmaei, S.; Liu, Z.; Zhou, W.; Zou, X.; Shi, G.; Lei, S.; Yakobson, B.I.; Idrobo, J.C.; Ajayan, P.M.; Lou, J. Vapour phase growth and grain boundary structure of molybdenum disulphide atomic layers. *Nat. Mater.* **2013**, *12*, 754–759. [CrossRef]
58. Hyun, C.-M.; Choi, J.-H.; Lee, S.W.; Park, J.H.; Lee, K.-T.; Ahn, J.-H. Synthesis mechanism of MoS_2 layered crystals by chemical vapor deposition using MoO_3 and sulfur powders. *J. Alloy. Compd.* **2018**, *765*, 380–384. [CrossRef]
59. Liu, H.; Bin Yang, R.; Yang, W.; Jin, Y.; Lee, C.J. Atomic layer deposition and post-growth thermal annealing of ultrathin MoO_3 layers on silicon substrates: Formation of surface nanostructures. *Appl. Surf. Sci.* **2018**, *439*, 583–588. [CrossRef]
60. Pondick, J.V.; Woods, J.M.; Xing, J.; Zhou, Y.; Cha, J.J. Stepwise sulfurization from MoO_3 to MoS_2 via chemical vapor deposition. *ACS Appl. Nano Mater.* **2018**, *1*, 5655–5661. [CrossRef]
61. Kim, H.; Ovchinnikov, D.; Deiana, D.; Unuchek, D.; Kis, A. Suppressing Nucleation in Metal–Organic Chemical Vapor Deposition of MoS_2 Monolayers by Alkali Metal Halides. *Nano Lett.* **2017**, *17*, 5056–5063. [CrossRef]
62. Zhou, D.; Shu, H.; Hu, C.; Jiang, L.; Liang, P.; Chen, X. Unveiling the Growth Mechanism of MoS_2 with Chemical Vapor Deposition: From Two-Dimensional Planar Nucleation to Self-Seeding Nucleation. *Cryst. Growth Des.* **2018**, *18*, 1012–1019. [CrossRef]
63. KaiáLee, M. Large-area few-layered graphene film determination by multispectral imaging microscopy. *Nanoscale* **2015**, *7*, 9033–9039.
64. Lu, M.-Y.; Wu, S.-C.; Wang, H.-C. Time-evolution of the electrical characteristics of MoS_2 field-effect transistors after electron beam irradiation. *Phys. Chem. Chem. Phys.* **2018**, *20*, 9038–9044. [CrossRef]
65. Hsieh, Y.-P.; Wang, Y.-W.; Ting, C.-C.; Wang, H.-C.; Chen, K.-Y.; Yang, C.-C. Effect of Catalyst Morphology on the Quality of CVD Grown Graphene. *J. Nanomater.* **2013**, *2013*, 6. [CrossRef]
66. Park, B.; Lee, D.; Kim, H.-S.; Cho, Y.; Park, S.; Kim, C.; Lee, T.; Woo, D.H.; Kim, J.H. Synergetic enhancement in optical nonlinearity of Au nanoparticle decorated MoS_2 via interaction between excitonic and surface plasmon resonances. *Appl. Surf. Sci.* **2020**, *532*, 147486. [CrossRef]
67. Zhang, G.; Zhang, Z.; Xia, D.; Qu, Y.; Wang, W. Solar driven self−sustainable photoelectrochemical bacteria inactivation in scale−up reactor utilizing large−scale fabricable Ti/MoS_2/MoOx photoanode. *J. Hazard. Mater.* **2020**, *392*, 122292. [CrossRef]
68. Yuan, Y.; Wang, W.; Shi, Y.; Song, L.; Ma, C.; Hu, Y. The influence of highly dispersed Cu_2O-anchored MoS_2 hybrids on reducing smoke toxicity and fire hazards for rigid polyurethane foam. *J. Hazard. Mater.* **2019**, *382*, 121028. [CrossRef]
69. Lu, C.; Xuan, H.; Zhou, Y.; Xu, X.; Zhao, Q.; Bai, J. Saturable and reverse saturable absorption in molybdenum disulfide dispersion and film by defect engineering. *Photonics Res.* **2020**, *8*, 1512. [CrossRef]
70. Hao, X.-Y.; Bergh, J.; Brodin, O.; Heltman, U.; Mannervik, B. Acquired resistance to cisplatin and doxorubicin in a small cell lung cancer cell line is correlated to elevated expression of glutathione-linked detoxification enzymes. *Carcinogenesis* **1994**, *15*,1167–1173. [CrossRef]
71. Hammond, C.L.; Lee, T.K.; Ballatori, N. Novel roles for glutathione in gene expression, cell death, and membrane transport of organic solutes. *J. Hepatol.* **2001**, *34*, 946–954. [CrossRef]
72. Kang, Z.; Yan, X.; Wang, Y.; Bai, Z.; Liu, Y.; Zhang, Z.; Lin, P.; Zhang, X.; Yuan, H.; Zhang, X.; et al. Electronic Structure Engineering of Cu_2O Film/ZnO Nanorods Array All-Oxide p-n Heterostructure for Enhanced Photoelectrochemical Property and Self-powered Biosensing Application. *Sci. Rep.* **2015**, *5*, srep07882. [CrossRef] [PubMed]
73. Tang, J.; Kong, B.; Wang, Y.; Xu, M.; Wang, Y.; Wu, H.; Zheng, G. Photoelectrochemical detection of glutathione by IrO_2–Hemin–TiO_2 nanowire arrays. *Nano Lett.* **2013**, *13*, 5350–5354. [CrossRef]
74. Zang, Y.; Ju, Y.; Jiang, J.; Xu, Q.; Chu, M.; Xue, H. Cu^{2+}-Modulated in situ growth of quantum dots for split-type photoelectrochemical immunoassay of prostate-specific antigen. *Anal.* **2019**, *144*, 4661–4666. [CrossRef]
75. Zhu, Y.; Xu, Z.; Yan, K.; Zhao, H.; Zhang, J. One-Step Synthesis of CuO–Cu_2O Heterojunction by Flame Spray Pyrolysis for Cathodic Photoelectrochemical Sensing of l-Cysteine. *ACS Appl. Mater. Interfaces* **2017**, *9*, 40452–40460. [CrossRef] [PubMed]
76. Tran, M.H.; Cho, J.Y.; Sinha, S.; Gil Gang, M.; Heo, J. Cu_2O/ZnO heterojunction thin-film solar cells: The effect of electrodeposition condition and thickness of Cu_2O. *Thin Solid Film.* **2018**, *661*, 132–136. [CrossRef]